

## SPIN GENERATION

## Two-dimensional chiral perovskites with large spin Hall angle and collinear spin Hall conductivity

Ibrahim Abdelwahab<sup>1,2,†</sup>, Dushyant Kumar<sup>3,4,†</sup>, Tieyuan Bian<sup>5,†</sup>, Haining Zheng<sup>1</sup>, Heng Gao<sup>6</sup>, Fanrui Hu<sup>3</sup>, Arthur McClelland<sup>2</sup>, Kai Leng<sup>5</sup>, William L. Wilson<sup>2</sup>, Jun Yin<sup>5\*</sup>, Hyunsoo Yang<sup>3\*</sup>, Kian Ping Loh<sup>1\*</sup>

Two-dimensional hybrid organic-inorganic perovskites with chiral spin texture are emergent spin-optoelectronic materials. Despite the wealth of chiro-optical studies on these materials, their charge-to-spin conversion efficiency is unknown. We demonstrate highly efficient electrically driven charge-to-spin conversion in enantiopure chiral perovskites  $(R/S\text{-MB})_2(\text{MA})_3\text{Pb}_4\text{I}_{13}$  ( $\langle n \rangle = 4$ ), where MB is 2-methylbutylamine, MA is methylamine, Pb is lead, and I is iodine. Using scanning photovoltage microscopy, we measured a spin Hall angle  $\theta_{\text{sh}}$  of 5% and a spin lifetime of  $\sim 75$  picoseconds at room temperature in  $\langle n \rangle = 4$  chiral perovskites, which is much larger than its racemic counterpart as well as the lower  $\langle n \rangle$  homologs. In addition to current-induced transverse spin current, the presence of a coexisting out-of-plane spin current confirms that both conventional and collinear spin Hall conductivities exist in these low-dimensional crystals.

**T**wo-dimensional (2D) Ruddlesden-Popper perovskites (RPPs) have emerged as spin-polarizable materials for optoelectronic applications because of their large spin-orbit (SO) coupling and chirality-induced spin selectivity (1–4). Alternating layers of organic cations and inorganic anion cages create multiple quantum wells whose composition can be described by the stoichiometric formula  $(\text{RNH}_{3/2}\text{A}_{(n-1)}\text{B}_n\text{X}_{3n+1})$ , where R is a bulky monovalent organic cation, A is a small monovalent organic cation, B is a divalent metal cation, X is a halide, and  $n$  is the number of inorganic layers within each quantum well (5, 6).

The large SO coupling in 2D RPPs allows for the optical excitation of spin-polarized carriers with circularly polarized light (7). The strength of SO interactions in 2D RPPs can be tuned by selecting different organic ligands. For example, the presence of chiral organic molecules allows chirality to be transferred to the inorganic lattice through spatial or electronic interactions such as asymmetric hydrogen-bonding interactions, dipolar interactions, and orbital mixing, which breaks inversion symmetry and induces large Rashba–Dresselhaus SO fields (4, 8, 9). Such chiral crystals lack mirror symmetry, and this noncentrosymmetric structure gives rise to distinctive electronic band structures and spin textures that, in turn, influence the spin

Hall effect (SHE), in which spins are transported and accumulate on opposite surfaces of a sample carrying electric current. The interplay between the crystal's chirality and SO coupling results in intriguing spin transport phenomena that have potential applications in spintronics and quantum computing.

Charge carriers moving in strongly SO-coupled bands experience an effective magnetic field that causes spin-dependent deflections that generate spin currents. The charge-to-spin conversion can occur through the SHE as well as the Rashba–Edelstein effect (10, 11). In the conventional SHE, the relativistic SO force acting on the carriers creates a finite spin current that emerges in the transverse direction of the charge current. The SO interactions associated with the Rashba–Dresselhaus effects stem from the dipole field and inversion asymmetry at the atomic sites (12). These induced SO fields share common relativistic origins, which makes it challenging to experimentally disentangle their contributions in charge-to-spin conversion (13). An interplay of these effects in crystals with low symmetry can modify the spin texture and induce unconventional configurations of the charge-to-spin conversion (14).

The spin signal can be electrically detected as voltage (15) or photovoltage (16), or it can be optically observed as magneto-optic Kerr rotation (17) or circularly polarized photoluminescence (CP-PL) (18). The low electrical conductivity on 2D RPPs, typically on the order of  $10^{-5}$  to  $10^{-7}$  S  $\text{cm}^{-1}$ , creates challenges in characterizing spintronic-related parameters (19, 20), especially for lower- $\langle n \rangle$  homologs of lead (Pb)-based 2D RPPs with large bandgaps that limit the ability to electrically generate and detect spin currents in these crystals. To date, the detection of spin polarization in 2D RPPs has mainly relied on CP-PL (21, 22) and circular photogalvanic experiments (2, 23, 24).

Although these studies have demonstrated the generation of helicity-dependent spin currents by CP light, there has been a lack of quantitative measurement of electrically driven spin currents (i.e., current-induced spin polarization). Consequently, the spin Hall angle ( $\theta_{\text{sh}}$ ), expressed by the ratio of spin current density  $J_s$  to charge current density  $J_c$ , remains unknown.

Given the trend of decreasing bandgap in higher- $\langle n \rangle$  RPP homologs with increasing width of the quantum wells (25), we synthesized phase-pure 2D RPP crystals  $(S/R\text{-rac-MB})_2(\text{MA})_3\text{Pb}_4\text{I}_{13}$  ( $\langle n \rangle = 4$ ) (where MB is 2-methylbutylamine and MA is methylamine) to investigate current-induced spin polarization by using scanning photovoltage microscopy. Exfoliated flakes supported charge-to-spin conversion through both conventional (perpendicular) and unconventional (collinear) spin polarization to create spin Hall conductivity (SHC) components with in-plane and out-of-plane spin-polarization, respectively. The SO coupling, the spin lifetime ( $\tau_s$ ), and the magnitude of  $\theta_{\text{sh}}$  were strongly enhanced in the chiral S/R-RPP crystals compared with the racemic rac-RPP crystal. We found that  $\theta_{\text{sh}}$  had opposite signs for the S and R enantiomers, which is a hallmark of chirality transfer from the organic to inorganic sublattices. Additionally, unlike most pure Rashba semiconductors that exhibit only in-plane spin polarization, both experiments and density functional theory (DFT) calculations revealed out-of-plane spin polarization in these crystals. We attributed this component to a substantial Dresselhaus component in the spin texture, which arises from the chirality-induced bulk symmetry breaking.

## RPP synthesis and characterization

High-quality, millimeter-sized  $(S/R\text{-rac-MB})_2(\text{MA})_3\text{Pb}_4\text{I}_{13}$  ( $\langle n \rangle = 4$ ) crystals were synthesized by using a temperature-lowering crystallization method (see materials and methods for more details) (26). Figure 1 shows the configurations of the different crystals schematically. The bulk crystals were exfoliated into thin flakes and transferred onto quartz substrates for optical characterization and onto prepatterned Au electrodes for optospintronic measurements.

The chiral organic molecules reduce the symmetry to the noncentrosymmetric  $P1$  space group (SG 1) for the S-RPP crystal and the  $P2_1$  space group (SG 4) for the R-RPP crystal. The single-phase purity of the as-grown crystals was confirmed by absorption and PL measurements that revealed small Stokes shifts of  $<10$  nm (fig. S1) and the absence of defect-related peaks at low temperatures (fig. S2). Absorption measurements revealed that the crystals had a bandgap of  $\sim 1.92$  eV.

## Current-induced spin accumulation

Charge and spin currents are linked through a third-order SHC tensor. The allowed components

<sup>1</sup>Department of Chemistry, National University of Singapore, Singapore 117543, Singapore. <sup>2</sup>Center for Nanoscale Systems, Harvard University, Cambridge, MA 02138, USA.

<sup>3</sup>Department of Electrical and Computer Engineering, National University of Singapore, Singapore 117576, Singapore.

<sup>4</sup>Department of Physics, Netaji Subhas University of Technology (NSUT), Dwarka, New Delhi 110078, India.

<sup>5</sup>Department of Applied Physics, Hong Kong Polytechnic University, Hung Hom, Kowloon, Hong Kong SAR.

<sup>6</sup>Department of Physics, Shanghai University, Shanghai 200444, China.

\*Corresponding author. Email: jun.yin@polyu.edu.hk (J.Y.); eleyang@nus.edu.sg (H.Y.); chmlhkp@nus.edu.sg (K.P.L.)

†These authors contributed equally to this work.

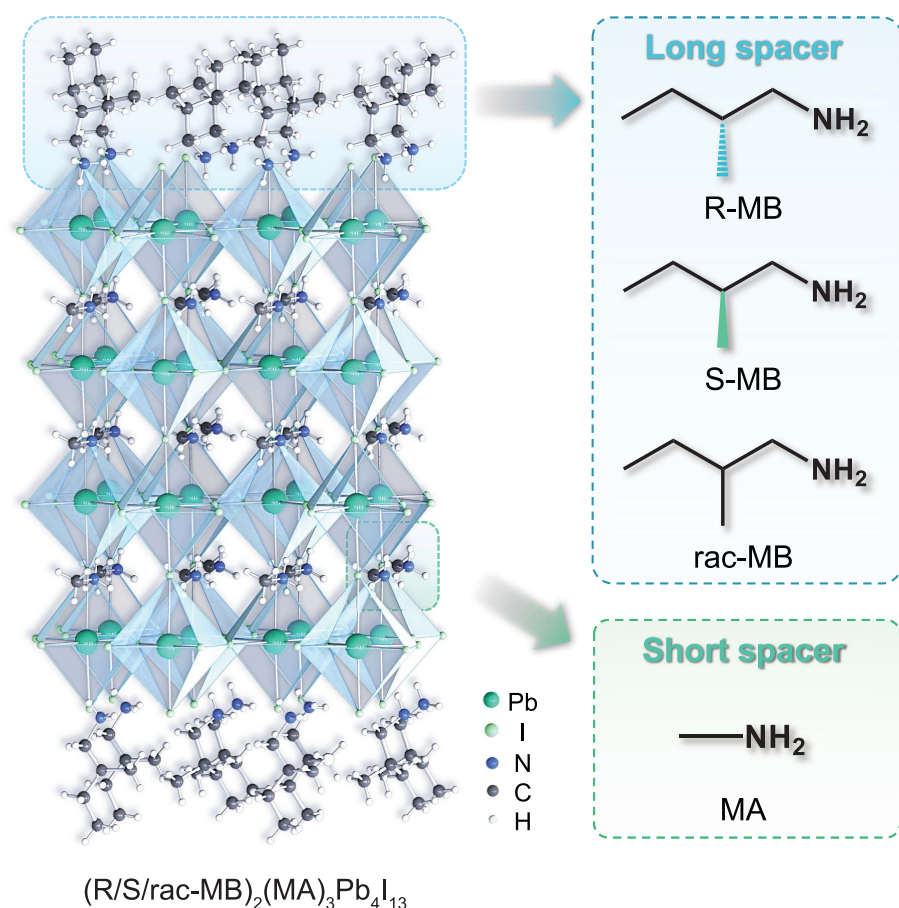


**Fig. 1. Molecular structure of  $\langle n \rangle = 4$  S/R/rac-RPPs.** Schematic showing a side view of  $\langle n \rangle = 4$  S/R/rac-RPP monolayer along the vertical axis. Turquoise, light green, blue, black, and white spheres denote Pb, I, N, C, and H atoms, respectively.  $\text{NH}_2$ , amine.

of the SHC tensor for the symmetry-reduced chiral crystals can be determined through symmetry analysis. Whereas SG 1 permits all 27 independent SHC components, SG 4 allows for 13 independent SHC components (14). For conventional SHC, the charge current direction  $k$  is transverse to both spin current direction  $j$  and spin polarization  $i$ , with the corresponding SHC tensor component denoted as  $\sigma_{jk}^i$  where  $i \neq k \neq j$ . For unconventional collinear SHC components, the charge and spin currents are orthogonal, and the spin polarization is aligned either with the charge current or with the spin current direction. In the latter case, the corresponding SHC tensor component is denoted as  $\sigma_{jk}^i$  when  $j \neq k$  and  $i$  is equal to  $j$  or  $k$ , e.g.,  $\sigma_{jk}^j$ . Generally, the unconventional components of the SHC tensors manifest only in low-symmetry crystals that have few symmetry operations.

To study the charge-to-spin conversion, we used scanning photovoltage microscopy to image the spin accumulation induced by currents at room temperature (see materials and methods, supplementary note S1, and fig. S3 for more details). In our apparatus (Fig. 2A), we

applied a DC voltage ( $V_{\text{sd}}$ ) in the longitudinal direction to drive  $J_c$  along the sample channel. To probe the spin populations, we scanned a CP laser beam that is incident normal to the surface of the perovskite sheets (16, 27). In the case of the SHE or Rashba-Edelstein effect with in-plane spin texture, the momentum conservation forbids an optically induced transfer of angular momentum for normally incident light (29). Thus, the normally incident light generates a helicity-dependent photovoltage (HDP) only when there is an out-of-plane spin component in the spin texture. To measure an HDP signal free from background photothermal or photovoltaic noise, typically present in conventional circular photogalvanic techniques, we modulated the helicity instead of the intensity of our laser light at a fixed frequency using a photoelastic modulator. Lock-in techniques were then used to collect the HDP signal, which appears as the first harmonic of the modulated polarization-dependent photovoltages; the details are provided in supplementary note S1. In the presence of electrical bias, current-induced out-of-plane spins accumulate near the two edges of the device channel

with opposite helicity. The presence of spin-accumulation generated a nonzero HDP signal, defined by  $V_{\text{HDP}} = V_{\text{LCP}} - V_{\text{RCP}}$ , where  $V_{\text{LCP}}$  and  $V_{\text{RCP}}$  are the photovoltages generated by left circularly polarized (LCP) and right circularly polarized (RCP) light. The sign and magnitude of the HDP signal provided information on the local spin polarization distribution.

As a validation step, we used this method to assess  $\theta_{\text{sh}}$  and  $\tau_s$  in heavy metals such as platinum (Pt) and topological insulators such as  $\text{Bi}_2\text{Se}_3$ . The obtained values aligned well with those determined through spin-pumping techniques, as detailed in table S1. Subsequently, we used this technique to investigate  $\langle n \rangle = 4$  RPP crystals. Figure 2B shows the optical image of a two-probe  $\langle n \rangle = 4$  S-RPP device with a single crystalline flake of 100-nm thickness before encapsulation. Figure 2C shows the flake after it is covered with a thin, transparent hexagonal boron nitride (<10 nm) layer as a protective layer against photo-oxidation. As an internal control, we compare the HDP signals of  $\langle n \rangle = 4$  chiral S and R-RPPs, which validated the chirality-dependent reversal of the sign of the current-induced spin signals in the two chiral crystals.

Scanning HDP maps of the device at different  $V_{\text{sd}}$  values are shown in Fig. 2, D to F. The left and right edges of the perovskite channel are indicated with black dashed lines, which were accurately determined through simultaneous reflection measurements (fig. S4). The maps displayed pronounced HDP signals at a bias voltage of  $V_{\text{sd}} = \pm 0.4$  V, whereas no HDP signal was observed in the absence of the electrical bias. On reversing the bias current direction (indicated with a black arrow), the spin polarization switched sign, exhibiting opposite signs at the two edges, in accordance with an electrically driven charge-to-spin conversion process.

In addition to the edge spin-accumulation HDP signal associated with conventional SHC tensor component  $\sigma_{yx}^z$ , we observed spin-accumulation HDP signal at the center of the channel (Fig. 2, D and F), which indicates the presence of the out-of-plane spin on the surface. We attributed this surface signal to a spin current that diffuses perpendicularly to the biased current along the out-of-plane direction with out-of-plane spin polarization. Such an unconventional SHC component with collinear spin polarization has been reported for low-symmetry Weyl semimetals  $1T'\text{-MoTe}_2$  and  $T_d\text{-WTe}_2$  (29–33) and is allowed in 2D perovskites with  $P1$  and  $P2_1$  symmetries (14). The collinear SHC component observed here for S/R-RPPs (i.e.,  $\sigma_{zx}^z$ ) has spin polarization parallel to the spin current, which is favorable for switching the perpendicular anisotropy magnetization without the help of an external magnetic field (34). In the same measurement setup, our reference Pt (SG 225) devices showed

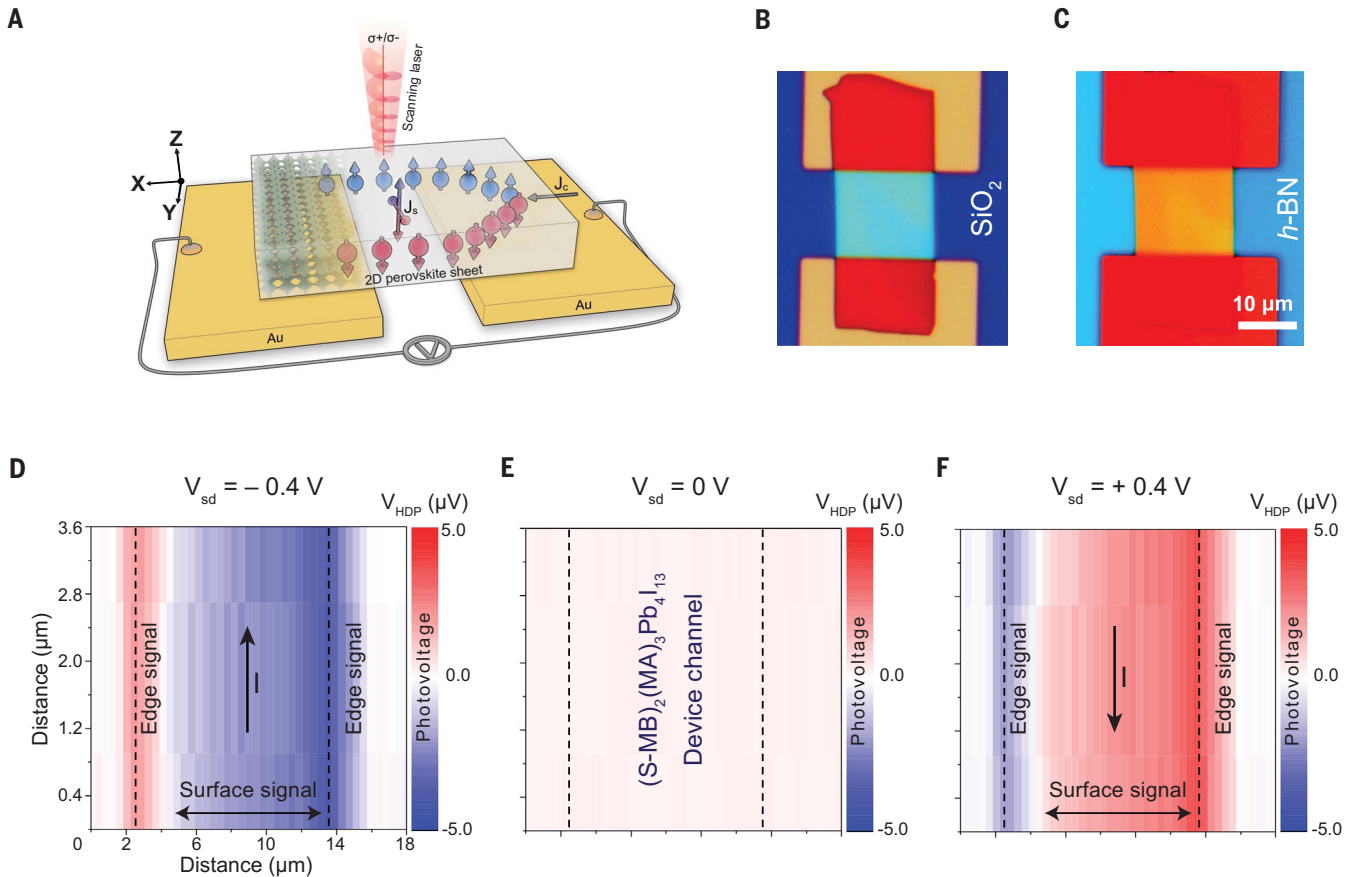


**Fig. 2. Current-induced spin accumulations in single-crystalline  $\langle n \rangle = 4$  S-RPP.**

(A) Schematic of the helicity-dependent scanning photovoltage microscope, in which the laser beam is scanned across the perovskite device channel to probe the local spin polarization distribution. The spin state can be determined from the sign of the HDP signal. (B) Optical image of two-probe  $\langle n \rangle = 4$  S-RPP device.  $\text{SiO}_2$ , silicon dioxide. (C) Optical image of the same device after encapsulation with hexagonal boron nitride (h-BN). (D to F) Spatially resolved 2D HDP maps of the  $\langle n \rangle = 4$  S-RPP device collected at bias voltages of (D)  $-0.4$  V, (E)  $0$  V,

and (F)  $+0.4$  V. The solid black arrows show the direction of the applied bias current. The black dashed lines indicate the left and right edges of the perovskite device channel. Blue and red colors indicate spin-up and spin-down signals, respectively. The maps show multidirectional charge-to-spin conversion in the  $\langle n \rangle = 4$  2D RPP: (i) conventional SHC tensor component (perpendicular spin polarization) that gives rise to the edge spin signal and (ii) unconventional SHC tensor component (collinear spin polarization) that gives rise to the surface spin signal.

only spin-polarized edge states (fig. S5) as expected from their conventional SHE with no collinear or longitudinal SHC components. In contrast to the chiral crystals, racemic  $\langle n \rangle = 4$  rac-RPP devices exhibited much weaker HDP signals (fig. S6), which is indicative of a weaker charge-to-spin conversion.

The edge and surface spin-accumulation signals of  $\langle n \rangle = 4$  chiral S-RPP devices exhibited a linear increase with the bias voltage magnitude (Fig. 3A). Negligible HDP signals were observed in the absence of bias voltage, which implies that the spin signal was a result of current-induced spin polarization. Hanle spin precession experiments were conducted at room temperature to assess the spin dynamics in  $\langle n \rangle = 4$  RPP devices, in which an in-plane magnetic field is applied to the RPP devices. Figure 3B shows the normalized edge and surface HDP signals of  $\langle n \rangle = 4$  S-RPP device

plotted against the applied magnetic field.  $\tau_s$  was approximated from the curve fitting to the Hanle precession theoretical formula  $A_1/[1 + (\Omega\tau_s)^2]$ , where  $A_1$  is the peak of HDP and  $\Omega = g\mu_B B_{\text{ext}}/\hbar$ ;  $g$  is the g-factor (fig. S7),  $\mu_B$  is the Bohr magneton,  $B_{\text{ext}}$  is the applied magnetic field, and  $\hbar$  is the reduced Planck constant. A small magnetic field applied perpendicular to the spin direction initiates spin precession at the Larmor frequency, which results in spin dephasing. We estimated a room temperature  $\tau_s$  of  $\langle n \rangle = 4$  S-RPP of 75 ps for the edge spins and 70 ps for the surface spins. Similarly, for racemic  $\langle n \rangle = 4$  rac-RPP, the edge and surface spin lifetimes were 44 and 40 ps, respectively (fig. S8).

We found that the  $\tau_s$  of  $\langle n \rangle = 4$  RPPs was much longer than those of heavy metals and topological insulators [ $\text{Bi}_2\text{Se}_3$ , 3.3 ps;  $\text{BiSbTeSe}_2$ , 18.6 ps; Pt, 0.57 ps; and  $\text{IrMn}_3$  (001), 1 ps]

(27, 35, 36). Scattering by impurities, defects, and grain boundaries reduces spin lifetime; thus, much shorter  $\tau_s$  values have been reported for polycrystalline hybrid perovskite samples such as achiral  $\langle n \rangle = 1$  RPP ( $0.24 \pm 0.01$  ps),  $\langle n \rangle = 4$  RPP (3.1 ps), and hybrid  $\text{CH}_3\text{NH}_3\text{PbI}_3$  perovskites ( $\sim 4$  ps) at room temperature (37, 38). Furthermore, the chiral  $\langle n \rangle = 4$  RPPs showed a stronger  $V_{\text{HDP}}$  signal and a longer  $\tau_s$  compared with the lower  $\langle n \rangle$  homologs as well as Pb bromide-based ferroelectric achiral perovskite  $\langle n \rangle = 2$   $(\text{BA})_2(\text{MA})\text{Pb}_2\text{Br}_7$  [BA, butylammonium ( $\text{C}_4\text{H}_9\text{NH}_3$ )] (SG 36) (figs. S9 to S11).

We attributed the relatively long spin lifetime in  $\langle n \rangle = 4$  RPPs to the interplay between Rashba splitting and phonon scattering (39). Using electron spin resonance spectroscopy (fig. S7), we determined that the g-factor values of our crystals were similar to the g-factor value of free electrons. Thus, the  $\Delta g$  spin-mixing



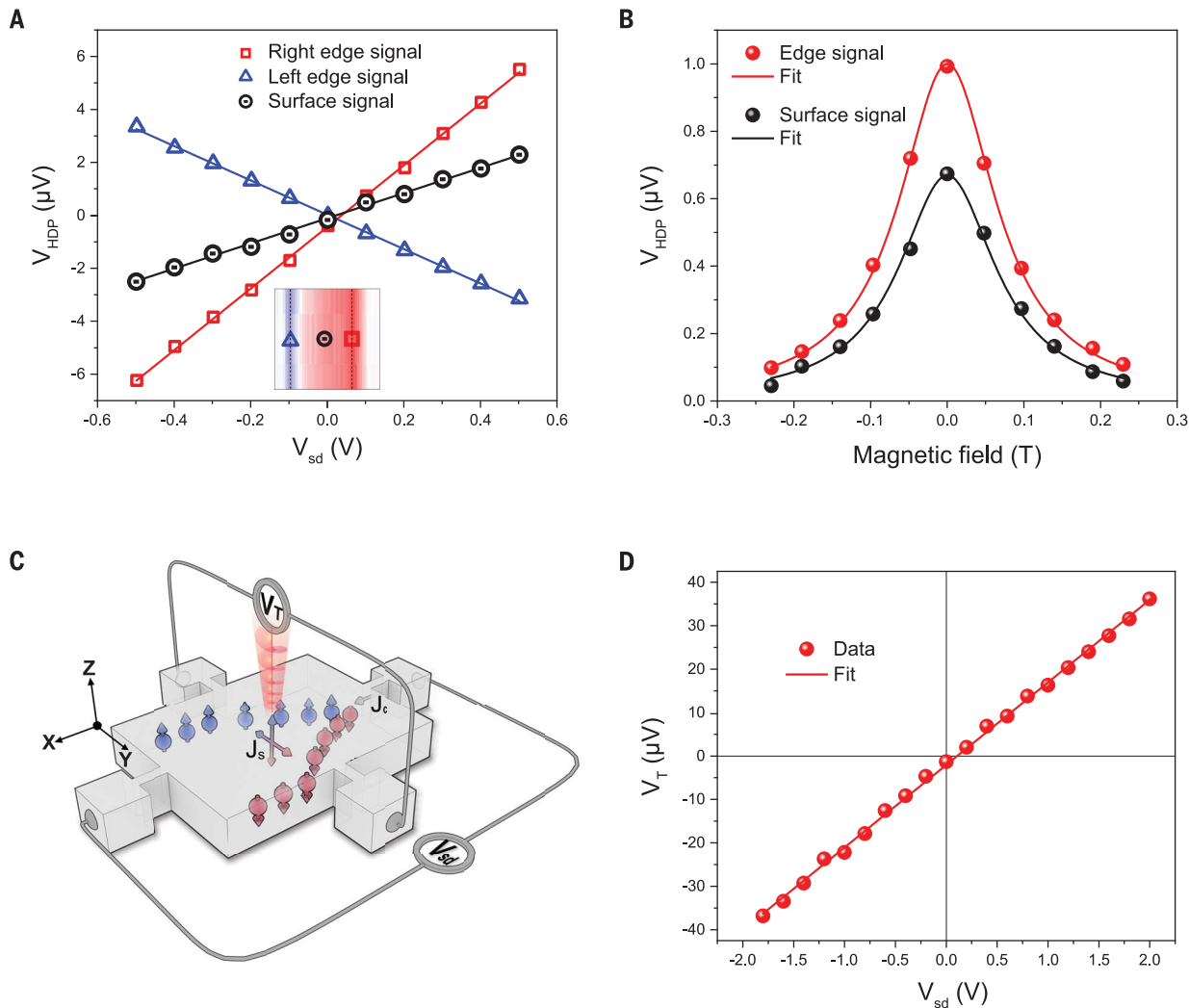


**Fig. 3. Characterization of current-induced spin accumulations in single-crystalline  $\langle n \rangle = 4$  S-RPP.** (A) Bias voltage dependence of  $V_{\text{HDP}}$  measured by fixing the laser spot at the left edge, the center, and the right edge of the  $\langle n \rangle = 4$  S-RPP device. (B) Measurement of the normalized edge and surface  $V_{\text{HDP}}$  signals as a function of the applied in-plane magnetic field. (C) Schematic of the Hall measurements in which the spin-dependent transverse voltage  $V_T$  is measured as a function of the bias voltage  $V_{\text{sd}}$  while fixing the laser beam at the center of the Hall cross for the quantitative determination of the spin Hall angle. (D) Bias voltage dependence of  $V_T$ . Solid lines are fits.

mechanism was not relevant to our single-crystalline 2D perovskite systems, which means that different dissociation rates for the spin-pair in the singlet and triplet spin configuration that may modulate the photocurrent did not contribute to the measured signal (40).

### Spin Hall angle measurements

We determine  $\theta_{\text{sh}}$  of the perovskite samples by using standard Hall bar devices (Fig. 3C). In this experiment, we detected the spin-dependent transverse voltage ( $V_T$ ) in the presence of longitudinal charge current. Our Hall-bar devices were subjected to CP light incident perpendicular to the sample. The laser spot was fixed at the center of the Hall cross to excite out-of-plane spin-polarized carriers that accelerated under the longitudinal electric field  $E_{\parallel}$  and generated the  $V_T$  signal through the inverse SHE (41).

We ruled out the spin-independent components by treating the  $V_T$  under linearly polarized light illumination as background and subtracting it.  $V_T$  can be defined in terms of  $\theta_{\text{sh}}$  as  $V_T = \theta_{\text{sh}} \rho_N w J_c P$ , where  $\rho_N$  is the resistivity of the sample (fig. S12),  $w$  is the device channel width, and  $P$  is the carrier spin polarization.  $P$  was calculated by using the equation  $P = GP_0\tau_s/n_e$ , which incorporates the initial spin polarization  $P_0$ , the optically excited electron density rate  $G$ , and the total electron density  $n_e$ .  $P_0$ , calculated from DFT, along with experimental values of  $G$ ,  $\tau_s$ , and  $n_e$  (supplementary note S2), were used to calculate  $P$ .

For  $\langle n \rangle = 4$  S-RPP devices,  $V_T$  reached 35  $\mu\text{V}$  under a bias voltage of 2 V (Fig. 3D), which resulted in a spin Hall angle  $\theta_{\text{sh}}$  (S-RPP) of 0.05 (5% charge-to-spin conversion efficiency). This value is larger than the values obtained by using the same technique for  $\theta_{\text{sh}}$  (Pt) =

0.0085 and  $\theta_{\text{sh}}$  ( $\text{Bi}_2\text{Se}_3$ ) = 0.0084 (16, 27). As a control study, we also tested racemic  $\langle n \rangle = 4$  RPP devices, which exhibited a much lower  $V_T$  of  $\sim 1.65 \mu\text{V}$  under a bias voltage of 5 V (fig. S13) and yielded a much lower  $\theta_{\text{sh}}$  (rac-RPP) of  $\sim 0.0017$  as compared with its chiral counterpart. This difference agrees with the expectation that chirality breaks bulk inversion symmetry and increases the inversion-asymmetric SO field strength, thereby promoting efficient charge-to-spin conversion. At lower temperatures, a notable enhancement in spin lifetime is anticipated, which results in extended spin diffusion lengths and increased spin Hall angles (24, 42–44).

### Lattice chirality effects

The SO coupling effects in 2D lead iodide RPPs primarily originate from the inorganic sublattice, consisting of Pb 6s and I 5p states at

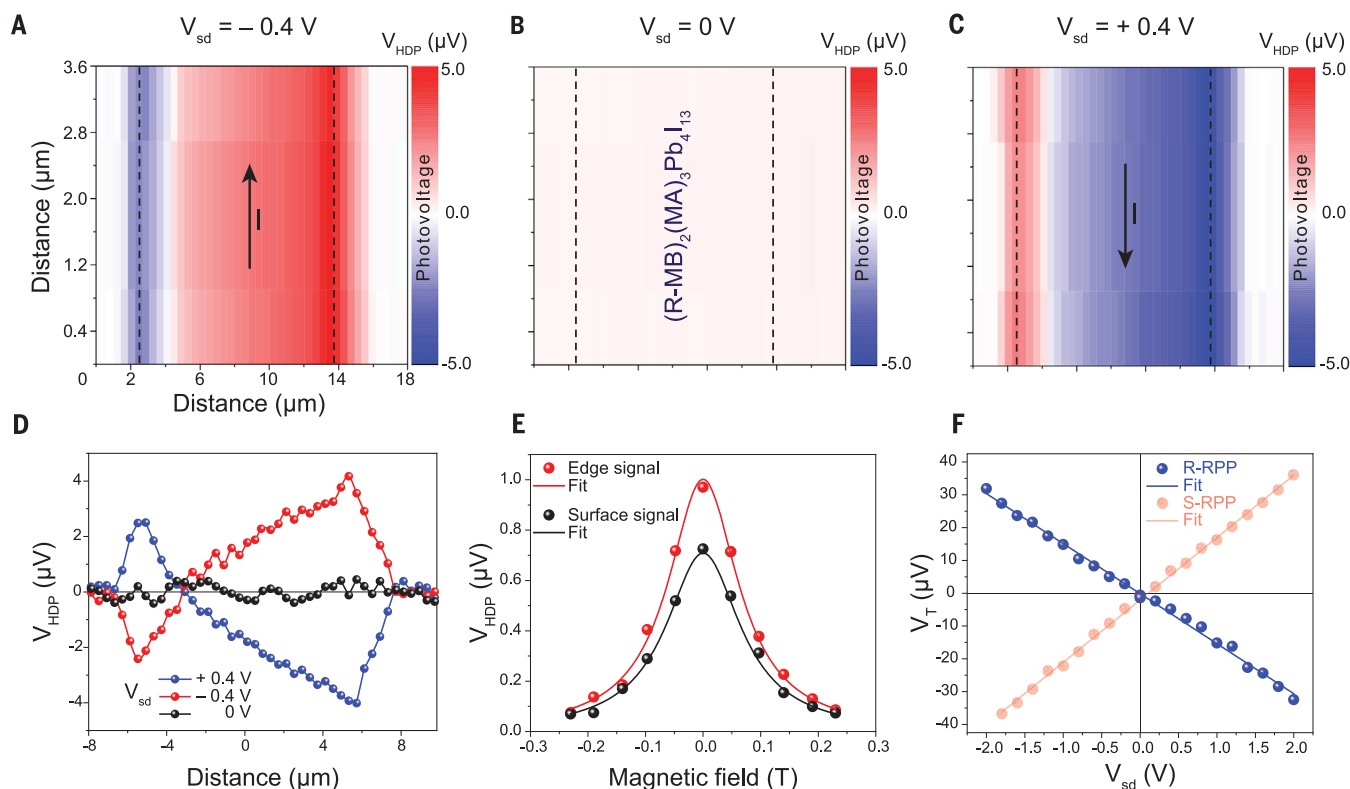


**Fig. 4. Characterization of current-induced spin accumulations in  $(n) = 4$  R-RPP.** (A to C) Two-dimensional HDP maps displaying the current-induced spin accumulation in an  $(n) = 4$  R-RPP device under bias voltages of (A)  $-0.4$  V, (B)  $0$  V, and (C)  $+0.4$  V. (D) One-dimensional HDP line profiles across the  $(n) = 4$  R-RPP channel. (E) Measurement

of the normalized edge and surface  $V_{HDP}$  signals as a function of the applied in-plane magnetic field. (F) Bias voltage dependence of the spin-dependent transverse voltage  $V_T$ . Solid lines are fits. The bias voltage dependence of  $V_T$  of  $(n) = 4$  S-RPP is shown as a transparent orange curve for comparison.

the top of the valence band and Pb 6p states at the bottom of the conduction band. However, the asymmetric hydrogen-bonding interactions of the chiral spacer cations, S(-) - or R-(+)-MB with the lead iodide octahedral cages result in helical distortions that break the symmetry of the inorganic lattice. By contrast, these lattice distortions are absent when a racemic mixture of organic spacers is used. We compared the spin-current diffusion direction for an  $(n) = 4$  S-RPP crystal and  $(n) = 4$  R-RPP crystal when driven by a charge current of the same sign. The 2D HDP maps of  $(n) = 4$  R-RPP devices under different bias voltages are shown in Fig. 4, A to C. The edge and surface  $V_{HDP}$  signals of R-RPP were comparable with those of S-RPP (Fig. 3A) at the same bias voltage value, but their signs were opposite, which was consistent with the opposite spin texture of R- and S-RPP. The opposite sign was also seen in the 1D HDP line profiles across the channel in Fig. 4D. The edge and surface spin lifetimes of R-RPP are 76 and 72 ps, respectively, as determined from the Hanle curves in Fig. 4E. Unlike the S-RPP with positive spin Hall angles, the R-RPP crystal exhibited a negative spin Hall angle  $[\theta_{sh}(\text{R-RPP}) \text{ of } -0.045]$ , as demonstrated in Fig. 4F, which

thus confirms that tuning chirality of the hybrid perovskite crystal changes the helicity of the spin current.

The chirality transfer results in opposite spin textures for the spin sub-bands between  $(n) = 4$  S-RPP and R-RPP. To gain an insight into the spin-band splitting and spin texture in both  $(n) = 4$  S-RPP and R-RPP crystals, we performed DFT calculations using monolayer models at the generalized gradient approximation (GGA)/Perdew-Burke-Ernzerhof (PBE) level with the incorporation of van der Waals interactions and SO coupling. The calculated electronic bands (Fig. 5, A and B) demonstrate that both crystals exhibited greater band splitting along the  $\Gamma \rightarrow X$  direction compared with the  $\Gamma \rightarrow Y$  direction.

Figure S14 illustrates how the reciprocal ( $k$ -) space band splitting is related to the real space. Notably,  $(n) = 4$  S-RPP exhibited larger splitting energy (20.1 meV) in comparison with  $(n) = 4$  R-RPP (15.0 meV). This difference could be attributed to the asymmetric interoctahedral tilting distortions present in the chiral crystals. The in-plane bond angle disparity ( $\Delta\beta_{in}$ ) connected with asymmetric tilting distortions of the surface metal halide octahedra was  $13.87^\circ$  and  $13.41^\circ$  for S-RPP versus  $5.38^\circ$  and  $5.26^\circ$  for

R-RPP (fig. S15). In the case of R-RPP, stronger hydrogen-bonding interactions between the  $\text{NH}_3^+$  group of the organic cation and the inorganic lattice with an average H-bond strength of 0.290 eV stabilized the surface octahedra and further reduced the in-plane surface distortion more effectively compared with S-RPP with an average H-bond strength of 0.257 eV (figs. S16 and S17). The calculated spin-band splitting energy increased concomitantly with the  $(n)$  number (figs. S18 and S19), in qualitative agreement with the measurements. The splitting energies of the spin sub-bands in MB-based chiral RPP crystals were larger than those in methylbenzylammonium-based chiral crystals (fig. S20).

Figure 5, C and D, illustrate the 2D spin textures for the components of  $S_x$ ,  $S_y$ , and  $S_z$  in both crystals. The spin components polarized parallel to the laboratory  $x$ - $y$  plane are termed in-plane spin components ( $S_x$  and  $S_y$ ), whereas the out-of-plane spin component ( $S_z$ ) is along the  $z$ -axis. In both cases, the in-plane spin components were minuscule compared with the out-of-plane spin components, which we ascribed to in-plane symmetry breaking induced by the chiral organic spacers (45, 46). This result agrees with the experiments in which we

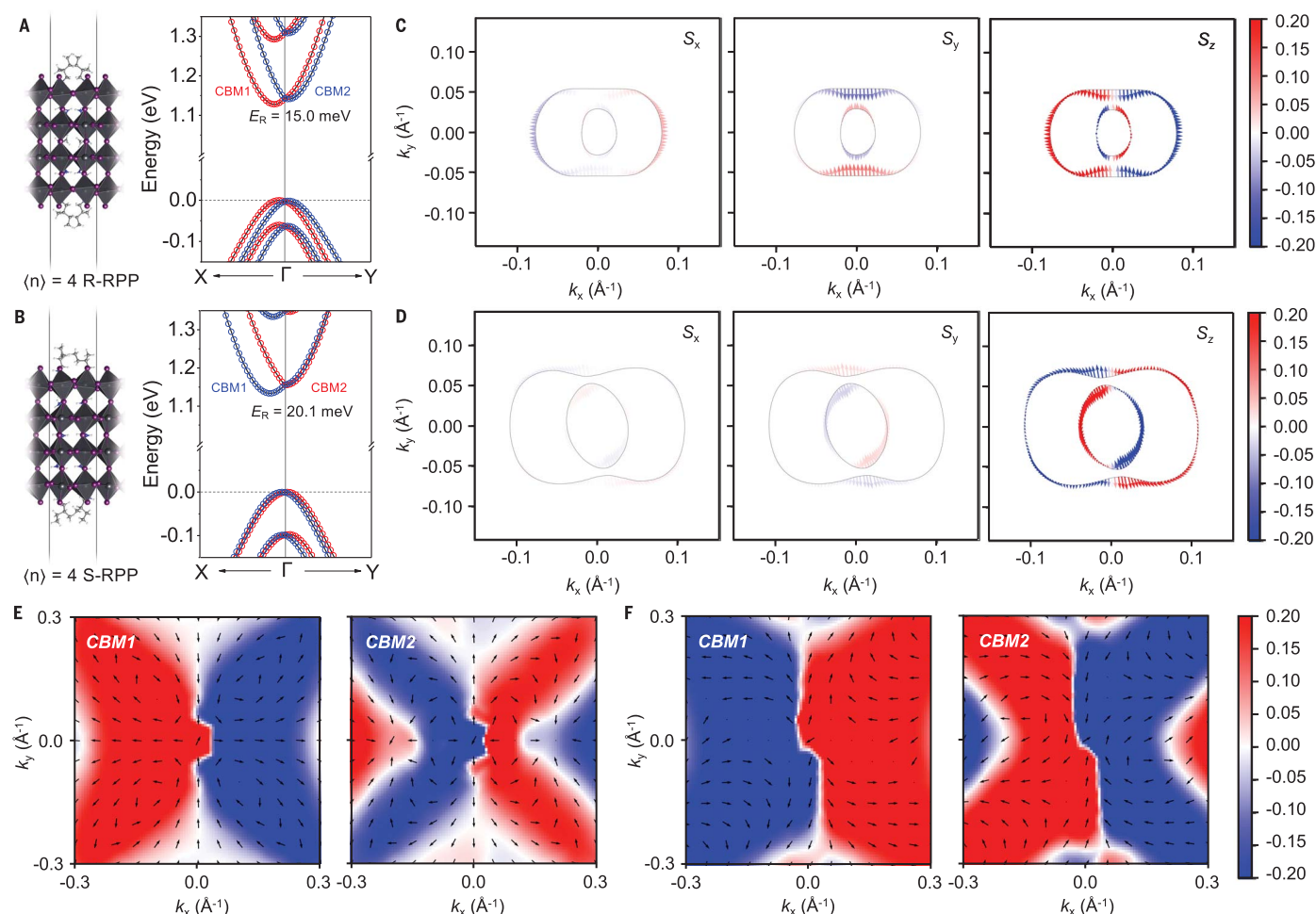


**Fig. 5. DFT calculations.** (A and B) Optimized crystal structures and calculated electronic bands of the (A)  $\langle n \rangle = 4$  R-RPP monolayer and (B)  $\langle n \rangle = 4$  S-RPP monolayer. (C and D) Two-dimensional spin textures for the projection components ( $S_x$ ,  $S_y$ , and  $S_z$ ) along the in-plane  $\Gamma \rightarrow X$  and  $\Gamma \rightarrow Y$  paths obtained at the energy surface of  $E = E_F + 0.95$  eV for (C)  $\langle n \rangle = 4$  R-RPP and (D)  $\langle n \rangle = 4$  S-RPP monolayers. The arrows indicate the spin direction, and the color represents the degree of spin polarization (the spin-up and spin-down

components are represented by blue and red colors, respectively). (E and F) Two-dimensional spin textures of conduction bands projected on the  $k_x$ - $k_y$  plane for CBM1 and CBM2 of (E)  $\langle n \rangle = 4$  R-RPP and (F)  $\langle n \rangle = 4$  S-RPP monolayers. The arrows indicate the in-plane spin components ( $S_x$  and  $S_y$ ). The blue and red colors represent the degree of spin-up and spin-down of the out-of-plane spin component ( $S_z$ ). The DFT calculations were performed at GGA-PBE + van der Waals with SOC.

detected the spin current with out-of-plane spin polarization.

Moreover, switching the chirality of the organic spacers from R to S switched the spin orientations for all three spin components between  $\langle n \rangle = 4$  R-RPP and  $\langle n \rangle = 4$  S-RPP. As shown in Fig. 5, E and F, the spin texture of the conduction band minimum inner (CBM1) and outer (CBM2) branches around the  $\Gamma$  point suggested that Rashba and Dresselhaus spin-momentum couplings were simultaneously present in both crystals, as evidenced by the tangential and radial character of the textures (46, 47).

To quantitatively evaluate the contributions of the Rashba and Dresselhaus effects, we further calculated the Dresselhaus parameter ( $\lambda_D$ ) and the Rashba parameter ( $\lambda_R$ ) by fitting the energy dispersions for both CBM1 and CBM2

using the  $k \cdot p$  Hamiltonian model (refer to the computational methods and table S2 for more details; the fitting lines are shown in fig. S21). In both crystals, the calculated  $\lambda_D$  values (4.88 eV·Å for R-RPP and 4.50 eV·Å for S-RPP) were much larger than the  $\lambda_R$  values (0.79 eV·Å for R-RPP and 1.28 eV·Å for S-RPP), which indicates that the pronounced band splitting is dominated by the Dresselhaus effect. The spin-split bands of  $\langle n \rangle = 4$  RPP crystals were verified experimentally through CP-PL measurements (supplementary note S3, figs. S22 and S23, and table S3).

### Discussion

In the context of Rashba-Dresselhaus spin splitting, our work demonstrates that chirality plays a crucial role in determining the strength and direction of SO coupling. The chirality transfer

from the organic to inorganic sublattices lowers the bulk symmetry of the crystal and introduces combined Rashba-Dresselhaus SO terms in the relativistic Hamiltonian. We observe bulk in-plane anisotropy in the SO coupling and unusual spin-dependent transport properties, such as unconventional SHE with out-of-plane spin polarization. Understanding and harnessing the SHE in such chiral crystals through chirality transfer has implications for developing new electronic and spintronic devices.

We have demonstrated current-driven non-equilibrium spin detection in hybrid enantiopure perovskite systems. Among different hybrid perovskite systems tested, we found that quasi-2D perovskites possessing chirality and high  $\langle n \rangle$  value (dimensionality) yielded the largest spin Hall angle and were competitive with reported inorganic topological insulators. In going

from  $\langle n \rangle = 1$  to  $\langle n \rangle = 4$  RPP, the spin signals increased in the higher homologs, and this increase was linked to their higher conductivities and SO field strengths. The sign of  $\theta_{\text{sh}}$  changed with the chirality of the organic cation used in the enantiopure perovskite, which thus evidenced the tuning of the spin texture in the inorganic lattice by chirality transmitted through organic–inorganic interlayer coupling. The chiral degree of freedom, coupled with a large spin Hall angle, confirmed that chiral perovskites provide a promising avenue for spin manipulation in prospective spintronic devices. By exploring the intricate interplay among crystal chirality, SO coupling, and spin transport in hybrid perovskites, we can uncover new ways to manipulate and control spins.

## REFERENCES AND NOTES

- H. Lu *et al.*, *Sci. Adv.* **5**, eaay0571 (2019).
- J. Wang *et al.*, *ACS Nano* **15**, 588–595 (2021).
- Y.-H. Kim *et al.*, *Science* **371**, 1129–1133 (2021).
- H. Lu *et al.*, *J. Am. Chem. Soc.* **142**, 13030–13040 (2020).
- Y. Chen *et al.*, *Adv. Mater.* **30**, 1703487 (2018).
- H. Tsai *et al.*, *Nature* **536**, 312–316 (2016).
- J. Even, L. Pedesseau, M. A. Dupertuis, J. M. Jancu, C. Katan, *Phys. Rev. B Condens. Matter Mater. Phys.* **86**, 205301 (2012).
- R. Naaman, Y. Paltiel, D. H. Waldeck, *Acc. Chem. Res.* **53**, 2659–2667 (2020).
- M. K. Jana *et al.*, *Nat. Commun.* **11**, 4699 (2020).
- J. Sinova, S. O. Valenzuela, J. Wunderlich, C. H. Back, T. Jungwirth, *Rev. Mod. Phys.* **87**, 1213–1260 (2015).
- A. Manchon, H. C. Koo, J. Nitta, S. M. Frolov, R. A. Duine, *Nat. Mater.* **14**, 871–882 (2015).
- X. Zhang, Q. Liu, J.-W. Luo, A. J. Freeman, A. Zunger, *Nat. Phys.* **10**, 387–393 (2014).
- T. D. Skinner *et al.*, *Nat. Commun.* **6**, 6730 (2015).
- A. Roy, M. H. D. Guimarães, J. Stawiriska, *Phys. Rev. Mater.* **6**, 045004 (2022).
- J. E. Hirsch, *Phys. Rev. Lett.* **83**, 1834–1837 (1999).
- J. Besbas *et al.*, *Adv. Opt. Mater.* **4**, 1642–1650 (2016).
- Y. K. Kato, R. C. Myers, A. C. Gossard, D. D. Awschalom, *Science* **306**, 1910–1913 (2004).
- J. Wunderlich, B. Kaestner, J. Sinova, T. Jungwirth, *Phys. Rev. Lett.* **94**, 047204 (2005).
- M. Safdari *et al.*, *J. Mater. Chem. A Mater. Energy Sustain.* **4**, 15638–15646 (2016).
- C. Ortiz-Cervantes, P. I. Román-Román, J. Vazquez-Chavez, M. Hernández-Rodríguez, D. Solís-Ibarra, *Angew. Chem. Int. Ed.* **57**, 13882–13886 (2018).
- J. Ma *et al.*, *ACS Nano* **13**, 3659–3665 (2019).
- G. Long *et al.*, *Nat. Photonics* **12**, 528–533 (2018).
- X. Liu *et al.*, *Nat. Commun.* **11**, 323 (2020).
- L. Zhang *et al.*, *Nat. Photonics* **16**, 529–537 (2022).
- K. Leng *et al.*, *Nat. Mater.* **17**, 908–914 (2018).
- C. C. Stoumpos *et al.*, *Chem. Mater.* **28**, 2852–2867 (2016).
- Y. Liu *et al.*, *Nat. Commun.* **9**, 2492 (2018).
- V. I. Belinicher, B. I. Sturman, *Sov. Phys. Usp.* **23**, 199–223 (1980).
- C. K. Safer *et al.*, *Nano Lett.* **19**, 8758–8766 (2019).
- J. H. Garcia *et al.*, *Phys. Rev. Lett.* **125**, 256603 (2020).
- P. Song *et al.*, *Nat. Mater.* **19**, 292–298 (2020).
- B. Zhao *et al.*, *Adv. Mater.* **32**, e2000818 (2020).
- S. Shi *et al.*, *Nat. Nanotechnol.* **14**, 945–949 (2019).
- Y. Liu *et al.*, *Nat. Electron.* **6**, 732–738 (2023).
- F. Dalla Longa, J. T. Kohlhepp, W. J. M. de Jonge, B. Koopmans, *Phys. Rev. B Condens. Matter Mater. Phys.* **81**, 094435 (2010).
- Y. Liu *et al.*, *Phys. Rev. Appl.* **12**, 064046 (2019).
- D. Giovanni *et al.*, *Adv. Sci. (Weinh.)* **5**, 1800664 (2018).
- G. Yumoto *et al.*, *Sci. Adv.* **8**, eabp8135 (2022).
- X. Chen *et al.*, *ACS Energy Lett.* **3**, 2273–2279 (2018).
- C. Zhang *et al.*, *Nat. Phys.* **11**, 427–434 (2015).
- N. Okamoto *et al.*, *Nat. Mater.* **13**, 932–937 (2014).
- P. Odenthal *et al.*, *Nat. Phys.* **13**, 894–899 (2017).
- Z.-G. Yu, Y. S. Li, J. Phys. Chem. C *Nanomater. Interfaces* **123**, 14701–14706 (2019).
- J. Wang *et al.*, *Nat. Commun.* **10**, 129 (2019).
- R. Xie *et al.*, *Phys. Rev. B* **107**, 155436 (2023).
- S. Bhattacharya, Y. Kanai, *Phys. Rev. Mater.* **7**, 055001 (2023).
- M. Kepenekian *et al.*, *ACS Nano* **9**, 11557–11567 (2015).

## ACKNOWLEDGMENTS

**Funding:** I.A. is supported by, and this work was performed in part at, the Harvard University Center for Nanoscale Systems (CNS), a member of the National Nanotechnology Coordinated Infrastructure Network (NNCI), which is supported by the National Science Foundation under NSF award no. ECCS-2025158. K.L.

acknowledges the Croucher Foundation (Croucher Tak Wah Mak Innovation fund) and the Research Grants Council of the Hong Kong Special Administrative Region, China (project nos. PolyU25305222 and PolyU15304623) and project no. 62322413 supported by the National Natural Science Foundation of China. J.Y. acknowledges funding support from the Hong Kong Polytechnic University (PolyU) (grant no. P0042930) and grants from the Research Grants Council of the Hong Kong Special Administrative Region, China (project nos. PolyU 25300823 and C4005-22Y). H.Y. is supported by Singapore's National Research Foundation (NRF) Investigatorship (NRF106-2020-0015). K.P.L. acknowledges Singapore's MOE Tier 2 grant no. MOE2019-T2-1-037 as well as Singapore's NRF Competitive Research Program CRP22-2019-0006. **Author contributions:** I.A., H.Y., and K.P.L. conceived the project and designed the experiments. I.A. performed micromechanical cleavage, 2D dry transfer, device fabrication, material characterization, and optical measurements under the supervision of W.L.W. and K.P.L.; D.K. designed the devices and performed helicity-dependent microscanning and Hanle and Hall measurements under the guidance of H.Y.; F.H. and I.A. helped in helicity-dependent microscanning and Hanle measurements. D.K. helped in device fabrication. T.B. performed the calculations and theoretical analysis under the supervision of J.Y.; H.G. contributed to the theoretical discussion. A.M. helped in optical characterization. H.Z. synthesized the racemic and chiral lead iodide-based crystals. K.L. synthesized the achiral lead bromide-based crystal. I.A. and K.P.L. wrote the manuscript. All authors discussed and analyzed the results and commented on the manuscript. **Competing interests:** The authors declare that they have no competing interests. **Data and materials availability:** All data are available in the main text or the supplementary materials. **License information:** Copyright © 2024 the authors, some rights reserved; exclusive licensee American Association for the Advancement of Science. No claim to original US government works. <https://www.science.org/about/science-licenses-journal-article-reuse>

## SUPPLEMENTARY MATERIALS

[science.org/doi/10.1126/science.adq0967](https://doi.org/10.1126/science.adq0967)  
Materials and Methods  
Supplementary Notes 1 to 3  
Figs. S1 to S23  
Tables S1 to S3  
Reference (48–71)

Submitted 26 April 2024; accepted 10 June 2024  
10.1126/science.adq0967